

Performance Analysis of DNN Inference/Training with Convolution and non-Convolution Operations

Hadi Esmailzadeh, Soroush Ghodrati, Andrew B. Kahng, Sean Kinzer,
Susmita Dey Manasi*, Sachin S. Sapatnekar, and Zhiang Wang

Abstract—Today’s performance analysis frameworks for deep learning accelerators suffer from two significant limitations. First, although modern convolutional neural network (CNNs) consist of many types of layers other than convolution, especially during training, these frameworks largely focus on convolution layers only. Second, these frameworks are generally targeted towards inference, and lack support for training operations. This work proposes a novel performance analysis framework, SimDIT, for general ASIC-based systolic hardware accelerator platforms. The modeling effort of SimDIT comprehensively covers convolution and non-convolution operations of both CNN inference and training on a highly parameterizable hardware substrate. SimDIT is integrated with a backend silicon implementation flow and provides detailed end-to-end performance statistics (i.e., data access cost, cycle counts, energy, and power) for executing CNN inference and training workloads. SimDIT-enabled performance analysis reveals that on a 64×64 processing array, non-convolution operations constitute 59.5% of total runtime for ResNet-50 training workload. In addition, by optimally distributing available off-chip DRAM bandwidth and on-chip SRAM resources, SimDIT achieves $18\times$ performance improvement over a generic static resource allocation for ResNet-50 inference.

Index Terms—Convolutional neural networks, Hardware accelerator, Performance simulator, Inference, Training.

I. INTRODUCTION

The success of using ASIC-based custom accelerator platforms in executing deep convolutional neural networks (DNNs/CNNs) has made them a prime choice as the computing platform for inference and training [1]. The design of optimized DNN accelerators involves a large design parameter space. A comprehensive performance analysis framework is crucial to explore this space and achieve optimized hardware performance from a large spectrum of design choices.

Modern DNN graphs, particularly for training, consist of many types of layers, e.g., convolution, non-linear activation, tensor addition for residual links, max pooling, average pooling, batch normalization, gradient computations with respect to input data and parameters, and multidimensional parameter tensor updates. While convolution layers are the largest single contributor to execution time during DNN execution, the combined contributions from layers other than convolution have non-negligible effects on the system-level performance of a network. During training, the energy and runtime overhead

from the large set of non-convolution layers can even exceed the energy and runtime for convolution layers (33%–52% energy and 30%–60% runtime overhead for ResNet-50, as demonstrated later in Section VII). Therefore, it is highly critical to develop simulation framework that models non-convolution layers along with convolution layer to enable accurate system-level performance analysis of DNN accelerators.

Prior works on DNN accelerator simulators do not comprehensively model all types of DNN layers while they target inference only and rarely have support for the training operations. For example, SCALE-Sim [2] develops an inference simulator for ASIC-based systolic accelerators that models convolution layers only. Timeloop [3], MAESTRO [4], and DeepOpt [5] propose DNN dataflow analysis frameworks for inference accelerators, but their evaluations focus only on convolution layers, and the work in [6] proposes an energy estimation model for the convolution operation only. While the modeling efforts in [7], [8] include pooling and tensor addition along with convolution, their scope is limited to inference and do not have support for training operations. TRIM [9] proposes a design space explorer for DNN training, but does not support batch normalization, a heavy training workload, and is not evaluated on mainstream ASIC accelerators [1], [10]–[13] that use systolic or vector dot-product style hardware.

Furthermore, prior convolution focused modeling efforts often suffer from inaccuracy and are inadequate for handling convolution operations during the training phase (discussed in Section V-B). For example, [2], [4] do not model the stall cycles due to off-chip communication, while [3] adopts a very simplified modeling approach for the DRAM stalls. This can lead to inaccurate estimation of runtime, especially during training where the operations are extremely memory-intensive. The works in [5], [7] do not support tiling across the kernel height-width dimensions. While this is acceptable for the inference phase, where kernel height \times width is quite small (i.e., lies between 1×1 to 11×11 for standard CNNs),

TABLE I: Inference and training operations modeled by SimDIT.

	Inference/ Forward pass of training	Backward pass of training		Section
Conv	Convolution	Gradient of loss w.r.t.	ifmap weight	IV-C,
	Fully-connected	Gradient of loss w.r.t.	ifmap weight	IV-D, V-B
non-Conv	Tensor-add	Gradient of loss w.r.t. input		IV-E
	ReLU activation Pool (max, avg, global avg)	Gradient of loss w.r.t. input Gradient of loss w.r.t. input		
non-Conv*	Batch normalization	Gradient of loss w.r.t.	input scale, shift	V-C
	–	Update of 1D, 2D, 4D	parameters	

*Training only

*Primary author

S. D. Manasi and S. S. Sapatnekar are with the Department of Electrical and Computer Engineering, University of Minnesota Twin Cities, Minneapolis, MN, USA. H. Esmailzadeh, S. Ghodrati, A. B. Kahng, S. Kinzer and Z. Wang are with the Department of Computer Science and Engineering, University of California San Diego, La Jolla, CA, USA.

it is not sufficient to handle the convolution operation during training where kernel height \times width can be very large (i.e., up to 223×223 during gradient computation for ResNet-50). Therefore, tiling across these kernel dimensions is necessary since they can be too large to fit in the on-chip memory.

This work proposes SimDIT, a comprehensive simulation framework for CNN inference and training for ASIC-based systolic DNN accelerator platforms. SimDIT comprehensively models convolution operations, including the attributes required to handle training, as well as a diverse set of non-convolution operations, thus enabling performance analysis and facilitating design space exploration of both convolution and non-convolution workloads of a network. We develop a generic tile-based template (discussed in Section IV-B) to abstract the computation of the layers. Our generic tile-based modeling strategy in SimDIT enables us to develop a tractable modeling framework that covers a large set of operations. A list of the operations/layers that are modeled by SimDIT to support CNN inference and training is summarized in Table I. The attributes of the layers are discussed in Sections IV-A and V-A. The source-code of SimDIT is publicly available [14].

II. GENERAL FRAMEWORK OF SIMDIT

Fig. 1 illustrates the general framework of SimDIT, our simulator for DNN inference and training for ASIC-based DNN accelerators. ASIC accelerator platforms comprise hardware components that execute operations within a DNN workload [1], [11], [15]. We classify these operations as:

- (1) *Conv*, in convolution and fully-connected (FC) layers.
- (2) *non-Conv*, in layers other than convolution, such as activation (e.g., using a rectified linear unit (ReLU)), pooling (Pool), tensor addition (Tensor-Add), batch normalization (BN), gradient computation, and parameter updates.

In SimDIT, we develop models to capture the execution behavior of both Conv and non-Conv hardware components of DNN accelerators. The modeling substrate of SimDIT is fully parameterizable in terms of a range of hardware attributes, e.g. size of the compute cores, bit-widths of each type of data, on-chip buffer sizes, and DRAM bandwidth at each off-chip interface. A full list of the parameterizable hardware attributes of SimDIT is presented in Table II while the details about the target hardware platforms are discussed in Section III.

Fig. 1 shows the high-level input and output interface of SimDIT. SimDIT takes two files (in .json format) as inputs:

- 1) a *Hardware Specifications* file that contains the specifications of the hardware attributes, and
- 2) a *DNN Specifications* file containing description for each layer of a DNN that includes information such as dimensions of all the input/output tensors, tile sizes of the tensors, order of execution loops, and datatypes.

Given the above specifications, SimDIT produces end-to-end *performance statistics* for executing the DNN on the hardware:

- **cycle counts:** number of on-chip cycles to perform the computations, DRAM stall cycles when the compute cores wait for data to be fetched from the off-chip memory, and total number of cycles to execute the network;

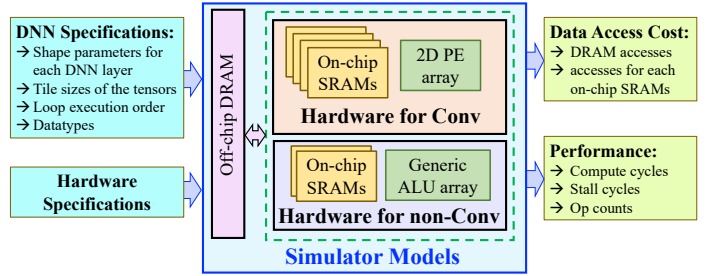


Fig. 1: General overview of SimDIT.

- **on-chip access counts:** access counts for each on-chip SRAM for each type of data;
- **off-chip access counts:** access counts for the DRAM for each type of data; and
- **op counts:** counts for each type of arithmetic operation.

The framework of SimDIT also includes energy and power computation module (discussed in Section VI) that combines backend data from post synthesized placed-and-routed designs with the *performance statistics* to compute end-to-end execution energy, power, and runtime of a DNN.

III. ASIC HARDWARE PLATFORM

Our target hardware platform is a general ASIC-based systolic DNN accelerator, similar to TPUv2 [1] and GeneSys [11]. Fig. 2 shows a system-level overview of the hardware architecture. The architecture consists of two key components: a systolic array for Conv and a SIMD array for non-Conv workloads. The SIMD array here is more versatile than in inference accelerators [12], [13] since it supports a diverse set of non-Conv operations that can execute DNN training.

The systolic array executes the convolution and FC layers. The layers comprise multiple types of data: ifmap, psum/ofmap, weight, and bias that are defined in Section IV-A. The systolic core consists of a $J\times K$ array of processing elements (PE). Each PE contains a MAC unit and pipeline registers to forward ifmap (horizontally) and psum (vertically) data to the adjacent PEs while the weight data is held locally within each PE. In each clock cycle, the PE array performs MAC operations between a $1\times J$ vector of ifmap and a $J\times K$ matrix of weight. During systolic execution, data in the ifmap vector flow horizontally (left to right) across columns and psums get accumulated vertically (top to bottom) across rows. After the pipeline is filled, the array produces a $1\times K$ vector of psum/ofmap every cycle. The systolic array has four on-chip buffers: IBuf, OBuf, WBuf, and BBuf for ifmap, ofmap/psum, weight, and bias data, respectively.

The SIMD array is a $1\times K$ ALU array that executes all non-convolution layers (ReLU, Pool, Tensor-add, BN, gradient computation, and parameter updates). The SIMD array is pipelined across each ALU: the pipeline stages are similar to a general MIPS processor where the K ALUs operate in parallel under a single instruction. The SIMD core is equipped with a vector memory (VMem) to store the input and output data as well as an instruction memory (IMem) to store the instructions. All six on-chip SRAMs of the systolic and SIMD cores

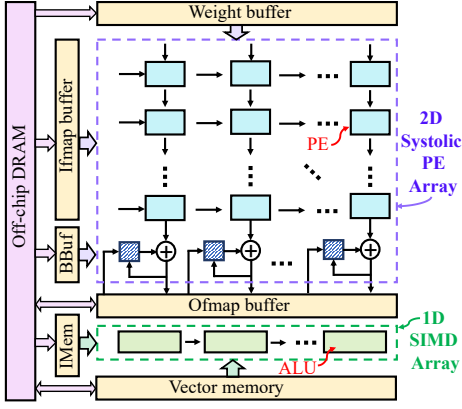


Fig. 2: Block diagram of the system-level hardware architecture.

TABLE II: Hardware configuration parameters.

Systolic array attributes	Notations	SIMD attributes	Notations
Number of PE rows, columns	J, K	Number of ALUs	K
Sizes of weight buffer, bias buffer	W_{buf}, B_{buf}	Size of vector memory	V_{mem}
Sizes of ifmap buffer, ofmap buffer	I_{buf}, O_{buf}	Size of instruction memory	I_{mem}
Bit-width of weight, bias	b_w, b_b	Bit-width of input	b_{in}
Bit-width of ifmap, psum/ofmap	b_i, b_p	Bit-width of output	b_{out}
DRAM bandwidth for weight and bias buffer	BW_w	DRAM bandwidth for vector memory	BW_v
DRAM bandwidth for ifmap buffer, ofmap buffer	BW_i, BW_o		
Number of cycles required for each type of arithmetic operation*			

*notations introduced as needed inside the text

communicate data with off-chip DRAM. Table II summarizes all the parameterizable attributes of the hardware platform.

IV. PERFORMANCE MODELS: INFERENCE

A. Basics of CNN Inference

Neural networks have two main types of phases: (i) training (Section V-A), when a network is trained to learn the model parameters, and (ii) inference, when a network is deployed for the target applications. Inference operations in a CNN primarily consists of Conv (convolution and FC) operations, nonlinear activation (e.g., ReLU), Tensor-add, and Pool layers.

Fig. 3 illustrates the convolution layer where a **filter** (or **weight**) tensor of size $(K_h \times K_w \times IC \times OC)$ is convolved with an input feature map (**ifmap**) of size $(IH \times IW \times IC)$. The computation produces an output feature map (**ofmap**) of size $(OH \times OW \times OC)$. During the computation, element-wise multiplication between each filter channel and a same-sized subregion of the corresponding ifmap channel (i.e., the orange ifmap region) produces intermediate partial sums (**psums**) that are accumulated across all IC channels to build elements in an ofmap channel (i.e., the purple ofmap element using the purple filter). Similar multiply and accumulate (MAC) operations are repeated using OC 3D filters while the filter slides through the ifmap with a stride S to build all the channels of a 3D ofmap. The correspondence between the filters and ofmap channels are shown by the color map. The batch size of the feature maps is shown by N where similar convolution computations are concurrently performed using N images. A convolution layer may include bias term of size OC that gets added with

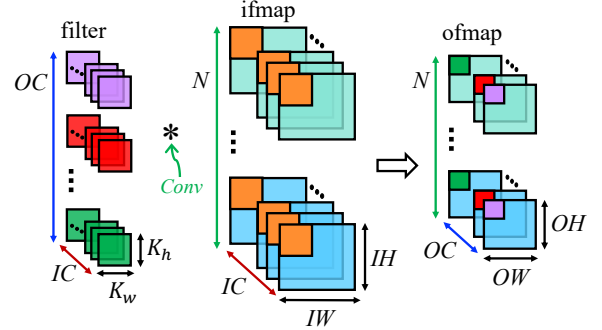


Fig. 3: Convolution layer illustrating filter, ifmap, and ofmap.

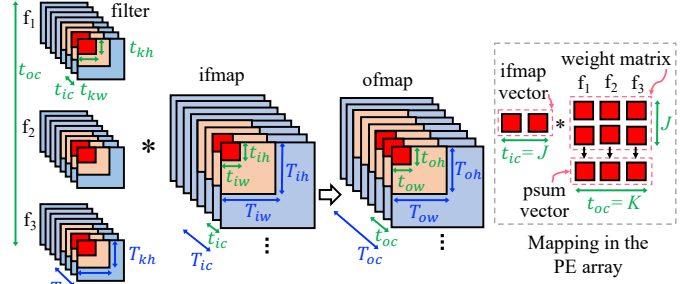


Fig. 4: A tiling template for a convolution layer. The tiling parameters for batch dimension, T_n and t_n , are omitted for simplicity.

each ofmap channel. An FC layer is similar to a convolution layer but has smaller tensor sizes and produces 1D ofmap.

Conv layers are optionally followed by ReLU, max/average pooling layers. A ReLU layer performs element-wise max operations on an input tensor and produces a same-sized output tensor. A Pool layer reduces the dimensionality of its input tensor where the computation involves max/average operations over a window of data while the window slides through each channel of the input tensor. CNNs that support residual learning (i.e., ResNet) contain shortcut connections that are realized by Tensor-add layers. The computation in a Tensor-add layer involves channel-by-channel element-wise addition, where the input and output tensors have same dimensions.

B. Generic Tile-based Template

We develop analytical models to obtain the end-to-end performance statistics for each CNN inference and training operation. Due to limited on-chip storage and parallel compute units (i.e., systolic PE array or SIMD ALUs) in a hardware, the computation of a layer is executed by dividing it into smaller subcomponents. We formulate a generic tile-based template that partitions the computation of each layer into *outer tiles* and *inner tiles*. For each tensor of a layer, inner tile computations are repeated to cover the outer tile while outer tile computations are repeated to process the entire layer. The outer tile has the volume of data that fits in the respective on-chip SRAM, while the inner tile has the volume of data processed by the compute units in one cycle.

Fig. 4 illustrates the concept of outer and inner tiles by showing the tiling template for a convolution layer. For each

type of data, light blue represents the full tensor volume, the orange region (nested within blue) illustrates the outer tile, and the red region (nested within orange) illustrates the inner tile. For each tensor, T_ϕ and t_ϕ denote the outer and inner tile sizes, respectively, for the dimensions ϕ where $\phi \in \{oh, ow, ih, iw, n, kh, kw, ic, oc\}$. Note that, our notational convention uses lower-case to indicate the *name of a dimension* while upper-case to denote the *size of a tensor along that dimension*. For example, oh is the name of the height dimension of ofmap while OH stands for the size of ofmap tensor along the height dimension.

DNN accelerators execute the convolution computation as a series of general matrix-vector multiplication (GEMM) operations [11], [15]. The right box of Fig. 4 shows how the computation in the inner tile is mapped as a GEMM operation to the systolic PE array of Fig. 2 to be processed in one cycle. The GEMM mapping of the convolution computation in the inner tile is performed by setting $t_{ic} = J$, $t_{oc} = K$, and all other inner tile parameters as 1 (i.e., $t_\phi = 1$ where $\phi \in \{oh, ow, ih, iw, n, kh, kw\}$). As shown in the right box, the $1 \times J$ ifmap vector is formed using one ifmap element from each of the J channels (i.e., the red region of the ifmap tensor). The $J \times K$ weight matrix is formed using K 3D filters where each column of the matrix consists of data from J channels of a single 3D filter (i.e., the red region of the filter tensors). Layers with small number of channels (i.e., $IC < J$, $OC < K$) are handled by zero padding the respective dimensions. The PE array performs the computation between the ifmap vector and weight matrix and produces K psums in one cycle (i.e., the red ofmap tensor region). A similar matrix-vector multiplication operation is repeated every cycle to process the outer tile. Once an outer tile is processed, the computed ofmap is moved to the DRAM and new outer tiles are loaded to the SRAMs. The process gets repeated until the entire layer is covered to produce the full ofmap volume.

We adopt similar tile-based templates to abstract the computation of each type of layer. Our generic tile-based template allows us to abstract the computation of all types of layers (as listed in Table I), thus enabling a tractable modeling framework that supports a large number of layers/operations.

C. Data Access Models for Conv: A Systolic Array Operation

DRAM access model: We first present our models to compute the data access cost for Conv layer, a layer executed in the systolic PE array (note that the Conv models presented in Sections IV-C and IV-D are used to handle Conv operations during the training phase as well, as outlined in Section V-B). We begin by computing the number of DRAM accesses for weight, ifmap, psum/ofmap, and bias data, denoted as A_{D_w} , A_{D_i} , A_{D_p} , and A_{D_b} , respectively. During the computation, outer tiles of ifmap, weight, and bias are loaded from the DRAM to their respective SRAMs. Irreducible psum tiles are stored [loaded] to [from] the DRAM as needed while the ofmaps are written back to DRAM once they are computed. The convolution computation proceeds along the seven convolution loops (i.e., $oh, ow, n, kh, kw, ic, oc$). We define seven

outer multipliers to express the iterations along each loop:

$$\begin{aligned} m_{oh} &= \frac{OH}{T_{oh}} ; m_{ow} = \frac{OW}{T_{ow}} ; m_n = \frac{N}{T_n} \\ m_{kh} &= \frac{K_h}{T_{kh}} ; m_{kw} = \frac{K_w}{T_{kw}} ; m_{ic} = \frac{IC}{T_{ic}} ; m_{oc} = \frac{OC}{T_{oc}} \end{aligned} \quad (1)$$

DRAM accesses for weight: Due to the large volume of weight data in CNNs, neural accelerators [10], [11] typically maximize weight data reuse after fetching them from the costly off-chip DRAM. Similarly, we execute convolution loops in a weight-stationary order (i.e., oh, ow, n are at the inner most loops) that maximizes weight data reuse. As shown in Fig. 4, the volume of outer tile for the weight, is given by

$$V_{w-tile}^o = \prod_{i \in \{kh, kw, ic, oc\}} T_i \quad (2)$$

Through the sliding window operation, we reuse the weight data across the height, width, and batch dimension of the feature maps. Therefore, the load of weight tile from the DRAM is iterated along the remaining four convolution loops, and the number of iterations along the four convolution loops is given by the product of the corresponding multipliers:

$$\mathcal{M}_{w-tile}^o = \prod_{i \in \{kh, kw, ic, oc\}} m_i \quad (3)$$

The number of total DRAM access for weight is then:

$$A_{D_w} = V_{w-tile}^o \times \mathcal{M}_{w-tile}^o \times b_w \quad (4)$$

Notice that Equation (4) leads to maximal weight reuse, where each weight data is loaded only once from the DRAM.

DRAM accesses for ifmap: Similar to the case above, we can write the volume of the outer tile for ifmap data as:

$$V_{i-tile}^o = \prod_{i \in \{ih, iw, n, ic\}} T_i \quad (5)$$

Since the weight data remains stationary, the load of ifmap tile from DRAM is repeated along all seven convolution loops as the computation proceeds along each loop where the number of iterations for ifmap data is given by the multiplier¹:

$$\mathcal{M}_{i-tile}^o = \prod_{i \in \{oh, ow, n, kh, kw, ic, oc\}} m_i \quad (6)$$

Thus, the total number of ifmap access from DRAM is:

$$A_{D_i} = V_{i-tile}^o \times \mathcal{M}_{i-tile}^o \times b_i \quad (7)$$

DRAM accesses for psum: Outer tile psum data volume is:

$$V_{p-tile}^o = \prod_{i \in \{oh, ow, n, oc\}} T_i \quad (8)$$

The psums are accumulated when the computation proceeds along the kh , kw , and ic dimensions, and the number of iterations corresponds to the product of the corresponding multipliers. To accumulate the psums generated from the current tile with the those from previous tiles, two operations (load and store) are required for each iteration, except for

¹SimDIT applies the ceiling operator on appropriate outer/inner multipliers to handle corner iteration cases for each data type. For readability, we omit the ceiling operators.

the first iteration that requires only one (store) operation. The multiplier for the access count over all outer tiles is thus:

$$\mathcal{M}_{p\text{-tile}}^o = \left(\prod_{i \in \{oh, ow, n, oc\}} m_i \right) \left(\left[\prod_{i \in \{kh, kw, ic\}} 2m_i \right] - 1 \right) \quad (9)$$

As before, we write the total psum DRAM accesses as:

$$A_{D_p} = V_{p\text{-tile}}^o \times \mathcal{M}_{p\text{-tile}}^o \times b_p \quad (10)$$

DRAM access for bias: To maximize bias data reuse, we execute convolution keeping oc at the outermost loop. After loading an outer tile of bias, T_{oc} , from the DRAM, this allows the addition of a bias element with all the ofmap elements in a 2D channel. Thus, each bias term is loaded once from the DRAM, and the number of DRAM accesses for bias data is:

$$A_{D_b} = T_{oc} \times m_{oc} \times b_b \quad (11)$$

SRAM access model: We now present our model to compute the number of SRAM accesses for weight, ifmap, psum/ofmap, and bias data, denoted as A_{S_w} , A_{S_i} , A_{S_p} , and A_{S_b} , respectively. In each clock cycle, the PE array reads inner tiles of weight and ifmap data from their respective SRAMs to perform the matrix-vector multiplication operation. The PE array also performs read and write access of inner tiles of psums from the ofmap buffer as needed. Similar to Equations (1), we define *inner multipliers* to express the iterations along the seven convolution loops to cover an outer tile as follows:

$$\begin{aligned} r_{oh} &= \frac{T_{oh}}{t_{oh}} ; r_{ow} = \frac{T_{ow}}{t_{ow}} ; r_n = \frac{T_n}{t_n} \\ r_{kh} &= \frac{T_{kh}}{t_{kh}} ; r_{kw} = \frac{T_{kw}}{t_{kw}} ; r_{ic} = \frac{T_{ic}}{t_{ic}} ; r_{oc} = \frac{T_{oc}}{t_{oc}} \end{aligned} \quad (12)$$

Furthermore, the number of inner iterations along the seven convolution loops to process a single outer tile of ofmap is computed by the multiplier, \mathcal{M}_{inner} , while the number of such outer iterations to cover the entire ofmap tensor is determined by the multiplier, \mathcal{M}_{outer} , as follows:

$$\mathcal{M}_{inner} = \prod_{i \in \{oh, ow, n, kh, kw, ic, oc\}} r_i \quad (13)$$

$$\mathcal{M}_{outer} = \mathcal{M}_{i\text{-tile}}^o \quad (14)$$

Since the PE array accesses the SRAMs during the computation of each inner tile that is nested within the outer tile, \mathcal{M}_{inner} along with \mathcal{M}_{outer} is needed to determine the number of SRAM accesses. In Table III, we summarize the computation of SRAM accesses associated with each type of data. The first column shows the volume of the inner tile, $V_{\alpha\text{-tile}}^i$, for each data type where $\alpha \in \{w, i, p, b\}$ indicating weight, ifmap, psum, and bias, respectively. The blue terms in parentheses in the second column represent the required multiplier to obtain the respective number of SRAM accesses.

For weight and ifmap, the PE array reads the inner tile volume of data every cycle, which is repeated along all seven convolution loops for both inner and outer iterations. Therefore, the multipliers for weight and ifmap account for these inner iterations nested within the outer iterations. The same process is applicable for the psum data where the

TABLE III: Computation of SRAM access count for each type of data for a Conv layer.

Data	Inner tile volume $V_{\alpha\text{-tile}}^i$	Number of SRAM accesses, A_{S_α}
weight	$\prod_{i \in \{kh, kw, ic, oc\}} t_i$	$V_{w\text{-tile}}^i \cdot (\mathcal{M}_{inner} \cdot \mathcal{M}_{outer}) \cdot b_w$
ifmap	$\prod_{i \in \{ih, iw, n, ic\}} t_i$	$V_{i\text{-tile}}^i \cdot (\mathcal{M}_{inner} \cdot \mathcal{M}_{outer}) \cdot b_i$
psum	$\prod_{i \in \{oh, ow, n, oc\}} t_i$	$\left[V_{p\text{-tile}}^i \cdot (2 \cdot \mathcal{M}_{inner} \cdot \mathcal{M}_{outer}) - (OH \cdot OW \cdot N \cdot OC) \right] \cdot b_p$
bias	-	$OH \cdot OW \cdot N \cdot OC \cdot b_b$

PE array performs both read and write access every cycle (i.e., $2 \times$ higher access than weight or ifmap). However, for each ofmap element, only write access is required when the associated psum is generated for the first time. The subtraction of the second term in the psum SRAM access expression incorporates this behavior. During the addition of bias data, the PE array reads a bias element from BBuf for each ofmap element. Therefore, the size of ofmap tensor directly provides the expression for bias SRAM access.

D. Cycle Count Models for Conv: A Systolic Array Operation

The total time to execute a layer is the sum of two components: (i) computation cycles and (ii) DRAM stall cycles.

Model for computation cycles: The number of MAC operations to process an outer tile is given by $(\prod_{i \in \{oh, ow, n, oc\}} T_i) \times (\prod_{i \in \{kh, kw, ic\}} T_i)$, where the term inside the second parenthesis represents the number of MAC operations associated with each ofmap location of the tile. Since the PE array performs $J \times K$ (i.e., $t_{ic} \times t_{oc}$, shown in Fig. 4) MAC operations in parallel, the number of cycles to compute an outer tile is given by (15), where the ic and oc dimensions are mapped along the rows and columns of the PE array, respectively.

$$\mathcal{C}_{tile}^{Conv} = \left(\prod_{i \in \{oh, ow, n, kh, kw\}} T_i \right) \times \left\lceil \frac{T_{ic}}{J} \right\rceil \times \left\lceil \frac{T_{oc}}{K} \right\rceil \quad (15)$$

The number of outer tiles required to process a Conv layer is given by the multiplier \mathcal{M}_{outer} (shown in Equation (14)). Thus, the total number of computation cycles for a layer is:

$$\mathcal{C}^{Conv} = \left[\mathcal{C}_{tile}^{Conv} + P_{SO_{SA}} \right] \times \mathcal{M}_{outer} \quad (16)$$

For each outer tile, $(J - 1) + (K - 1)$ initial cycles are required to fill the pipeline of the vertical and horizontal systolic execution in the PE array. This pipeline setup overhead per tile in the systolic array is denoted by $P_{SO_{SA}}$ in (16).

Model for DRAM stall cycles: Due to limited off-chip bandwidth, there are stall cycles when the PE array remains idle and waits for the data to be fetched from the DRAM. To reduce such stall cycles, all the buffers of the PE array (i.e., IBuf, OBuf, WBuf, and BBuf) are double-buffered, where the computation is overlapped with data load and store operations with the DRAM. Since DRAM stall cycles depend on the outer tiles only, in the context of DRAM stall modeling, we use to term *tile* to refer to the *outer tile*. As shown in Fig. 6(a), under the double buffered scheme, during the computation of j^{th} tile, the required data to compute the next tile is loaded while the generated data from the previous tile is stored.

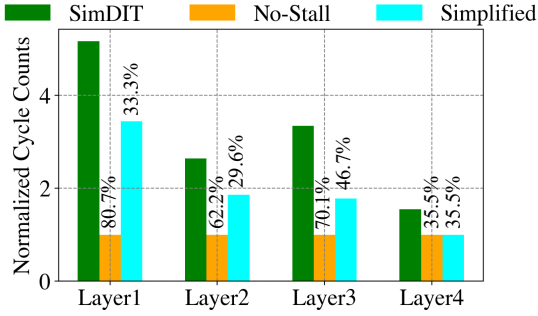


Fig. 5: Comparison of SimDIT cycle counts with No-Stall and Simplified cases using four Conv layers of ResNet-50 for both inference (Layer1, Layer2) and training (Layer3, Layer3) phases.

In a Conv layer, data load/store patterns from/to DRAM are different during the execution of various tiles. After loading from DRAM, a data tile can be reused across multiple subsequent tile computing segments, resulting in nonuniformity in the load-store pattern across tiles. For example, for a tile that requires the weights to be loaded, the memory operations during the computation are the weight load, ifmap load, psum load, and psum store. On the other hand, for another tile that reuses weights from the previous tile, the ifmap load, psum load, and psum store take place without a weight load operation. Due to these differences in the DRAM access pattern across different tiles, it is important to handle each *tile computing segment* with a *unique load-store pattern* separately to accurately estimate the DRAM stall cycles.

In Fig. 5, we illustrate the importance of a performance model that incorporates the hardware execution behavior at a tile-level granularity using quantitative examples. The figure compares SimDIT (a tile-level granular model) with two scenarios: (i) No-Stall: assumes zero DRAM stall cycles due to double buffering, (ii) Simplified: estimates overall cycle count using maximum of isolated execution cycles across total load/store and compute operations (i.e., maximum of four parallel components: total MAC computation cycles, total cycles for weight+bias access, total cycles for ifmap access, and total cycles for psum/ofmap access).

The cycles counts (normalized to No-stall case) are shown using four representative Conv layers of ResNet-50: Layer1 and Layer2 are from inference phase while Layer3 and Layer4 are from training phase (i.e., during backward pass). The layers are executed on inference and training hardware, respectively, with 64×64 PE array. The data is obtained using various breakdown of the performance statistics produced by SimDIT (i.e., computation cycles, DRAM stalls, and total off-chip access counts for each type of data). As can be seen from Fig. 5, No-stall and Simplified cases underestimate the cycle counts to a large degree leading to inaccurate performance estimation: up to 80.7% for No-stall while up to 46.7% for the Simplified case. Therefore, it is essential to adopt tile-level granular model that comprehensively captures the behavior of each tile computing segment.

In our weight-stationary execution of convolution loops, since the weight data remains stationary, movement of the other two types of data, *ifmap load* and *psum store*, takes place

TABLE IV: An exhaustive enumeration of three types of load/store operations. The last column marks the valid/invalid combinations.

Cases	<i>weight+bias load</i>	<i>weight load</i>	<i>psum load</i>	Validity
Case-1	0	0	0	✓
Case-2	0	0	1	✓
Case-3	0	1	0	×
Case-4	0	1	1	✓
Case-5	1	0	0	✓
Case-6	1	0	1	×
Case-7	1	1	0	×
Case-8	1	1	1	×

during the execution of all tiles. There are three remaining load/store operations, *weight+bias load* (load operation of weight and bias tile both), *weight load* (load operation of weight tile only without the load operation of bias tile)², and *psum load* (load operation of psum tile), that may or may not occur during the computation of a tile depending on the reuse of the respective data for that tile. Therefore, tile computing segments with unique load-store patterns are determined by the combinations of these three load/store operations. Exhaustive enumeration of these 3 operations gives 8 cases with unique load-store patterns. The properties of the cases are summarized in Table IV where, for each column, bit 1 [0] indicates that the corresponding load/store operation takes place [does not take place] during a tile computing segment. Now, 4 cases out of the 8 (indicated in the last column of the table) cannot occur during the execution of a tile due to the following properties:

- *weight+bias load* and *weight load* are mutually exclusive since weight load operation is already included within the operation where both weight and bias are being loaded. This makes Case-7 and Case-8 invalid.
- To maximize bias data reuse, the bias tile is loaded during the processing of the outermost *oc* loop (discussed under “DRAM access model” in Section IV-C) when the *kh*, *kw*, and *ic* loops (i.e, the dimensions along which psum is accumulated) go through their first iteration. Since the first iteration along these three loops does not have any previously generated psum to load, *psum load* and *weight+bias load* operations are mutually exclusive. This makes Case-6 invalid.
- *weight load* occurs when the computation proceeds along the *kh*, *kw*, and *ic* loops starting from the second iteration along these dimensions. Since for these computations, both load and store operations of psum are required to perform psum accumulation, Case-3, where *weight load* without an accompanying *psum load* occurs, is invalid.

A representation of the remaining four valid cases illustrating the parallel computation and load/store operations is shown in Fig. 6(b). For example, in Case-2, the *ifmap load*, *Compute*, and *psum store* can be carried out in parallel, but *psum load* must follow *psum store*. For each of these four valid cases, we calculate the number of times each case occurs (i.e., occurrence count, \mathcal{O}_{Case-i}) and the associated stalls per tile. For a single case, the per tile stall cycle is multiplied by the

²In standard CNNs, *bias load* is a small fraction of *weight load* operation. For example, for ResNet-50 inference on a 64×64 array, #of bias access from DRAM is two orders of magnitude lower than #of weight access. Despite this, we treat *weight+bias load* and *weight load* as separate cases for the completeness of the model.

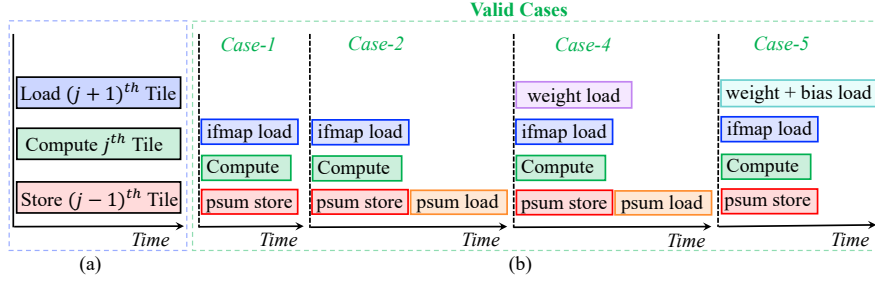


Fig. 6: (a) Illustration of parallel load, compute, and store operations of tiles. (b) Four unique load-store scenarios while processing convolution tiles.

occurrence count to obtain the total stall cycles for that case. Finally, the sum of stall cycles from all four cases provides the total DRAM stall cycles to fully process the Conv layer.

As an example, we illustrate the derivation of occurrence count and per tile stall cycle for one example case, Case-4.

Number of occurrences: As shown in Fig. 6(b), the unique attribute of Case-4 is the *weight load* operation, which only occurs in this case out of all cases in the figure. Therefore, the number of tile computing segments when *weight load* operation takes place provides the occurrence count for Case-4. As discussed in Section IV-C, the weight is reused along ow , oh , and n dimensions. Therefore, the number of tiles when weight data is loaded, regardless of bias load, is given by the multiplier \mathcal{M}_{w-tile}^o (Equation (3)).

The bias tiles are loaded, along with the weights, with the outermost oc loop. Hence, the number of tiles when *weight+bias load* takes place is given by m_{oc} . Now, by subtracting this from \mathcal{M}_{w-tile}^o , we obtain the number of tiles when *weight load* operation occurs. Therefore, the occurrence count for Case-4 is given by:

$$\mathcal{O}_{Case-4} = \mathcal{M}_{w-tile}^o - m_{oc} \quad (17)$$

Number of stall cycles per tile: The systolic PE array in Fig. 2 is equipped with separate off-chip interface for IBuf (which loads ifmap), OBuf (which loads and stores psum), and a shared interface for WBuf and BBuf (which loads weight and bias) to parallelly communicate data with the DRAM. For each case, Fig. 6(b) pictorially shows parallel load-store operations that are overlapped with each other and with the computation. Therefore, the number of stall cycles per tile for Case-4 is computed by taking the maximum among the time required to complete the respective parallel operations and given by:

$$\mathcal{S}_{tile-Case-4}^{Conv} = \max \left(\mathcal{C}_{tile}^{Conv}, \left\lceil \frac{V_{w-tile}^o b_w}{BW_w} \right\rceil, \left\lceil \frac{V_{i-tile}^o b_i}{BW_i} \right\rceil, \left\lceil \frac{2V_{p-tile}^o b_p}{BW_o} \right\rceil \right) \quad (18)$$

As defined in Table II, BW_w , BW_i , and BW_o are the DRAM bandwidth for weight, ifmap, and psum data, respectively.

The total stall cycles for Case-4 are now computed by taking the product of the occurrence count in (17) and the per-tile stall cycle count in (18). Following similar procedure, we compute the stall cycles associated with the other cases.

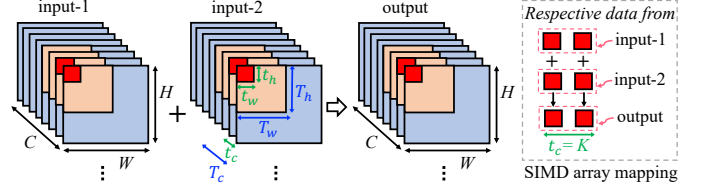


Fig. 7: Tensor-add layer illustrating the two inputs, output, and their notations. The notations for the batch dimension (i.e., batch size: N ; tiling parameters: T_n and t_n) are omitted for readability.

E. Models for Tensor-add (non-Conv) in the SIMD Array

We now present our data access and cycle count models for the Tensor-add layer, a representative layer executed on the SIMD array component of the hardware. Similar models are developed for other non-Conv inference operations. Fig. 7 shows our notations for the Tensor-add layer where element-wise addition between two inputs each with size $(H \times W \times N \times C)$ produces an output of the same dimension. The interpretation of the tiling template is similar to the approach discussed in Section IV-B where in Fig. 7, for each tensor, T_ϕ and t_ϕ indicate the sizes of outer and inner tile, respectively, for the dimension ϕ where $\phi \in \{h, w, n, c\}$. Since the SIMD array uses the vector memory to store all inputs and outputs of a layer, outer tiles from all inputs/outputs must fit in VMem. The right box in Fig. 7 illustrates the mapping of the computation in the inner tile (i.e., processed in one cycle) to the K ALUs of the SIMD array by setting $t_h = t_w = t_n = 1$, and $t_c = K$. Number of DRAM accesses: During the computation of Tensor-add layer, outer tiles of input-1 and input-2 are loaded from the DRAM to VMem while outer tiles of output are written back to DRAM as they are computed. Since the computation proceeds along the four computation loops (i.e., h, w, n, c), the number of outer iterations³ to cover the entire output tensor is given by:

$$\mathcal{M} = \frac{H}{T_h} \times \frac{W}{T_w} \times \frac{N}{T_n} \times \frac{C}{T_c} \quad (19)$$

For both the inputs as well as output, the volume of an outer tile, \mathcal{V}_{tile} , is given by $(T_h \times T_w \times T_n \times T_c)$. Each tile is

³Unlike Conv layer, Tensor-add layer does not have any data reuse property and the modeling approach is less intricate than the Conv layer (this is true for other non-Conv inference layers as well). Therefore, in order to avoid unneeded notational complexity, we present the Tensor-add models using the outer tiles only, and omit the use of superscript/subscript to differentiate between inner and outer components.

loaded/stored from/to DRAM once. Therefore, the number of DRAM access for the entire layer is computed by:

$$A_{D_{Tensor-add}} = \mathcal{V}_{tile} \times \mathcal{M} \times (2 \times b_{in} + b_{out}) \quad (20)$$

Number of SRAM accesses: For each outer tile of output, the number of arithmetic addition operations equals \mathcal{V}_{tile} since there is one addition operation for each output element. Besides, for each addition operation, two input operands are read from the VMem while one output operand is written to VMem. Therefore, the number of accesses for VMem, $A_{S_{Tensor-add}}$, for the entire layer is the same as in (20).

Number of computation cycles: The SIMD array performs K (i.e., $t_c = K$, shown in Fig. 7) addition operations in parallel where λ_{add} cycles are required to complete an addition operation per ALU. Therefore, the number of cycles to compute an outer tile is given by the following equation where the c dimension is mapped along the ALUs of the SIMD array:

$$\mathcal{C}_{tile}^{Tensor-add} = (T_h \times T_w \times T_n) \times \left\lceil \frac{T_c}{K} \right\rceil \times \lambda_{add} \quad (21)$$

Since the number of outer tiles to process the entire output tensor is given by the multiplier, \mathcal{M} , the total number of computation cycles for the Tensor-add layer is determined by (22). The SIMD array uses a 6-stage MIPS pipeline (i.e., instruction fetch, decode, address generation, data read, execution, and write back). In addition, the array is pipelined across the K ALUs. Therefore, at the beginning of the computation of each outer tile, the array requires $(6 - 1) + (K - 1)$ cycles to fill the pipeline. This pipeline setup overhead per tile, (PSO_{SIMD}), is incorporated in Equation (22).

$$\mathcal{C}^{Tensor-add} = \left[\mathcal{C}_{tile}^{Tensor-add} + PSO_{SIMD} \right] \times \mathcal{M} \quad (22)$$

Number of stall cycles: Since the data reuse opportunity in non-Conv layers (minimal to zero for most layers) is far less than Conv layers and VMem needs to fit tiles from all input and output tensors of a non-Conv layer, we adopt single buffering for the SIMD processor where data load/store operations with DRAM and computation take place sequentially. The SIMD array is stalled between the computation of each outer tile to load and store the respective outer tiles of data. As shown in (23), the associated stall cycles for the layer are computed by dividing the data volumes with the off-chip bandwidth for VMem (i.e., BW_v bits/cycle).

$$\mathcal{S}^{Tensor-add} = \left\lceil \frac{\mathcal{V}_{tile} \times (2 \times b_{in} + b_{out})}{BW_v} \right\rceil \times \mathcal{M} \quad (23)$$

V. PERFORMANCE MODELS: TRAINING

A. Basics of CNN Training

Standard CNN training algorithm adopts backpropagation with stochastic gradient descent (SGD) [16], [17]. The training method consists of many iterations of two main steps: forward pass and backward pass. The forward pass is functionally same as the inference phase where the computation advances from the first layer to the last layer of a network. The forward pass includes all the operations of the inference phase (i.e., inference is a subset of training). In addition, it also includes a BN layer that improves both training time and accuracy [18].

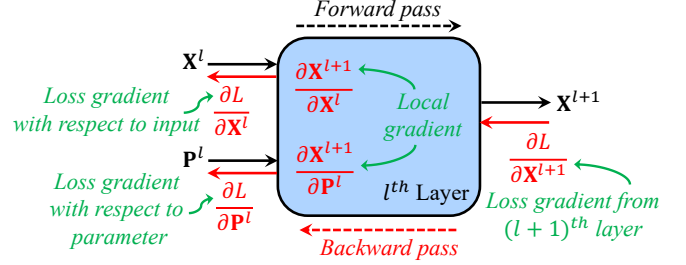


Fig. 8: Overview of computation for a layer during training.

During the backward pass, the network is run in reverse where the computation advances from the last layer to the first layer, and a set of errors (or loss values) computed using a loss function backpropagates through each layer of the network. Fig. 8 shows the computations involved for l^{th} layer during training. The computation between input \mathbf{X}^l and parameter \mathbf{P}^l produces the output \mathbf{X}^{l+1} during the forward pass. The backward pass performs the computation of gradient of loss (i.e., loss gradient) with respect to input ($\frac{\partial L}{\partial \mathbf{X}^l}$) and parameter ($\frac{\partial L}{\partial \mathbf{P}^l}$) using chain rule of differentiation as follows [19]:

$$\frac{\partial L}{\partial \mathbf{X}^l} = \frac{\partial L}{\partial \mathbf{X}^{l+1}} \cdot \frac{\partial \mathbf{X}^{l+1}}{\partial \mathbf{X}^l} ; \quad \frac{\partial L}{\partial \mathbf{P}^l} = \frac{\partial L}{\partial \mathbf{X}^{l+1}} \cdot \frac{\partial \mathbf{X}^{l+1}}{\partial \mathbf{P}^l} \quad (24)$$

Here, L is the loss function, $\frac{\partial L}{\partial \mathbf{X}^{l+1}}$ is the loss gradient propagated from the $(l+1)^{th}$ layer while $\frac{\partial \mathbf{X}^{l+1}}{\partial \mathbf{X}^l}$ and $\frac{\partial \mathbf{X}^{l+1}}{\partial \mathbf{P}^l}$ are local gradients of the l^{th} layer with respect to input and parameter, respectively. All bold notations indicate multidimensional tensors. Since $\frac{\partial L}{\partial \mathbf{X}^{l+1}}$ acts as an input for the l^{th} layer, the gradient expressions in (24) are self-contained where only the local gradients need to be determined which depend on the layer type. Similar to inference, each layer can be treated individually during the backward pass without the need for the information about the loss function or next/previous layer.

The computed loss gradient with respect to parameter is used to update the parameters of the layer while the loss gradient with respect to input gets propagated to the $(l-1)^{th}$ layer. Layers that do not have any parameter (i.e., ReLU, Pool, Tensor-add) exclude the computation of $\frac{\partial L}{\partial \mathbf{P}^l}$. As stated earlier, Table I summarizes the list of operations/layers required for CNN training along with inference.

B. Loss Gradients for Conv: Systolic Array Operations

The backward pass through the l^{th} Conv layer consists of two components: (i) computation of loss gradient with respect to ifmap tensor \mathbf{X}^l (i.e., $\frac{\partial L}{\partial \mathbf{X}^l}$) and (ii) computation of loss gradient with respect to weight tensor \mathbf{W}^l (i.e., $\frac{\partial L}{\partial \mathbf{W}^l}$). Standard implementations of these two components map the computation into Conv operation (i.e., the Conv operation during forward pass, shown in Fig. 3) by applying several tensor transformations.

Mapping $\frac{\partial L}{\partial \mathbf{X}^l}$ computation as Conv: Specifically, to compute $\frac{\partial L}{\partial \mathbf{X}^l}$, the following tensor transformations are applied:

- The elements in each channel of the input loss gradient tensor (i.e., $\frac{\partial L}{\partial \mathbf{X}^{l+1}}$) are dilated⁴ with $(S-1)$ zeros, both

⁴Dilation is the process of inserting zeros in between the elements of a tensor, which expands its size.

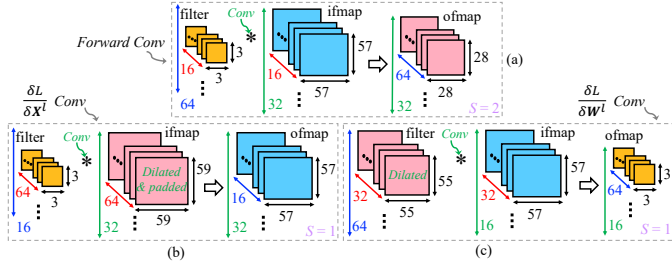


Fig. 9: Numerical example of Conv dimensions during training: (a) Forward Conv for the l^{th} layer, (b) Backward Conv to compute $\frac{\partial L}{\partial \mathbf{X}^l}$, and (c) Backward Conv to compute $\frac{\partial L}{\partial \mathbf{W}^l}$.

horizontally and vertically.

- The gradient $\frac{\partial L}{\partial \mathbf{X}^{l+1}}$ is also padded with $(K_h - 1)$ zeros at the top/bottom and $(K_w - 1)$ zeros at the left/right.
- The elements in each channel of the weight tensor (i.e., \mathbf{W}^l) are flipped horizontally and vertically.
- ifmap and ofmap channel dimensions are interchanged.

After these transformations, the computation of $\frac{\partial L}{\partial \mathbf{X}^l}$ (acts as **ofmap**) becomes a Conv operation with stride one (i.e., $S = 1$) between the transformed $\frac{\partial L}{\partial \mathbf{X}^{l+1}}$ (acts as **ifmap**) and \mathbf{W}^l (acts as **filter**) tensors.

Mapping $\frac{\partial L}{\partial \mathbf{W}^l}$ computation as Conv: The mapping of $\frac{\partial L}{\partial \mathbf{W}^l}$ as Conv involves the following tensor transformations:

- The transformation described at the first bullet for $\frac{\partial L}{\partial \mathbf{X}^l}$ computation is applied in $\frac{\partial L}{\partial \mathbf{X}^{l+1}}$ tensor.
- ifmap channel and batch dimensions are interchanged.

After these transformations, the computation of $\frac{\partial L}{\partial \mathbf{W}^l}$ (acts as **ofmap**) becomes a Conv operation with stride one between the transformed $\frac{\partial L}{\partial \mathbf{X}^{l+1}}$ (**filter**) and \mathbf{X}^l (**ifmap**) tensors.

The simulation framework of SimDIT requires only the size of each tensor of a Conv layer to predict the associated hardware *performance statistics*. Therefore, from the size of each tensor of a Conv layer during the forward pass (i.e., forward Conv), we calculate the sizes of the transformed tensors and supply that as inputs to SimDIT to determine the data access and cycle count costs for executing $\frac{\partial L}{\partial \mathbf{X}^l}$ and $\frac{\partial L}{\partial \mathbf{W}^l}$. Since the computations are Conv operations, we use our models from Sections IV-C and IV-D. The precise formulation to obtain the tensor sizes for the Conv operations corresponding to $\frac{\partial L}{\partial \mathbf{X}^l}$ and $\frac{\partial L}{\partial \mathbf{W}^l}$ (i.e., backward Conv operations) from the tensor sizes of the forward Conv is summarized in Table V and Fig. 9.

C. BN Loss Gradients: SIMD Array Operations (non-Conv)

As a representative non-Conv training operation, we present the modeling approach of SimDIT for batch normalization (BN) layer during backward pass. A similar modeling approach is adopted for all the non-Conv training operations listed in Table I. In the forward pass of l^{th} BN layer, computation using an input tensor, \mathbf{X}^l , of size $(H \times W \times N \times C)$ and a pair of parameter tensors, scale (γ^l) and shift (β^l) each of size C , produces BN transformed output. The backward pass through l^{th} BN layer (henceforth, we call it BN_{back}) consists of computing three components:

- loss gradient with respect to parameter scale, $\frac{\partial L}{\partial \gamma^l}$

TABLE V: Formulas showing the relationship among the dimension sizes of the forward Conv and backward Conv operations*.

Filter dimensions and stride	Additional ifmap/ofmap dimensions
For $\frac{\partial L}{\partial \mathbf{X}^l}$ computation as Conv	
$K_h^B = K_h^F$	$OH^B = IH^F$
$K_w^B = K_w^F$	$OW^B = IW^F$
$IC^B = OC^F$	$IH^B = S^F(OH^F - 1) + 1 + 2(K_h^F - 1)$
$OC^B = IC^F$	$IW^B = S^F(OW^F - 1) + 1 + 2(K_w^F - 1)$
$S^B = 1$	$N = N$
For $\frac{\partial L}{\partial \mathbf{W}^l}$ computation as Conv	
$K_h^B = S^F(OH^F - 1) + 1$	$OH^B = K_h^F$
$K_w^B = S^F(OW^F - 1) + 1$	$OW^B = K_w^F$
$IC^B = N^F$	$IH^B = IH^F$
$OC^B = OC^F$	$IW^B = IW^F$
$S^B = 1$	$N^B = IC^F$

*superscript F and B indicate dimension sizes for the forward and backward Conv, respectively.

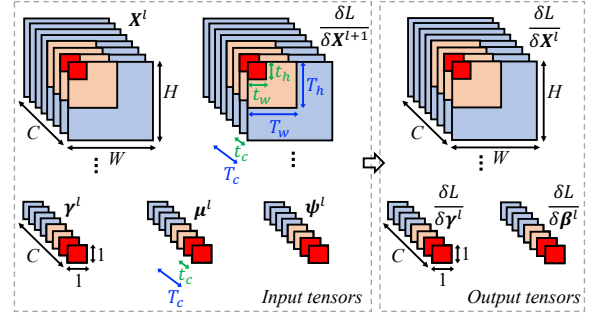


Fig. 10: Illustration of input and output tensors including their notations during the backward pass through l^{th} BN layer. The batch dimension of \mathbf{X}^l , $\frac{\partial L}{\partial \mathbf{X}^{l+1}}$, and $\frac{\partial L}{\partial \mathbf{X}^l}$ tensors and the associated notations (i.e., batch size: N ; tiling parameters: T_n and t_n) are omitted in the figure for better visualization.

- loss gradient with respect to parameter shift, $\frac{\partial L}{\partial \beta^l}$
- loss gradient with respect to input, $\frac{\partial L}{\partial \mathbf{X}^l}$

The left box of Fig. 10 shows the five tensors that are used as inputs for BN_{back} . The tensor μ^l denotes the batch mean and the tensor ψ^l represents the inverse square root of batch variance. Both of these tensors are computed during the forward pass of BN layer and stored off-chip to be used during the backward pass. The tensor $\frac{\partial L}{\partial \mathbf{X}^{l+1}}$ indicates the input loss gradient. The right box shows the three output tensors of BN_{back} . The dimensions of all the input and output tensors are visually shown in the figure. The interpretation of the tiling template is same as Fig. 7 (i.e., T_ϕ and t_ϕ stand for the sizes of outer and inner tile, respectively, for the dimension ϕ where $\phi \in \{h, w, n, c\}$). Outer tiles of all the input and output tensors are stored in VMem while the K ALUs of the SIMD array operate in parallel to process inner tile computations every cycle using $t_h = t_w = t_n = 1$, and $t_c = K$.

The analytical expressions [18] to compute the three outputs of BN_{back} are shown in Equations (26)-(28) where following standard implementations, analytical simplification is applied to obtain the expression for $\frac{\partial L}{\partial \mathbf{X}^l}$. The computations of the loss gradients use normalized form of the input tensor which is denoted by $\tilde{\mathbf{X}}^l$ and computed using (25). In BN_{back} , the operations inside nested h, w, n loops are same where these three dimensions act as the batch dimension with an effective batch size of $N_{\text{eff}} = (H \times W \times N)$. Therefore, for notational clarity in Equations (25)-(28), we use two indices to indicate

Algorithm 1 Steps to Compute Loss Gradients for l^{th} BN Layer

INPUT: Input tensors: $\mathbf{X}^l, \frac{\partial L}{\partial \mathbf{X}^{l+1}}, \boldsymbol{\gamma}^l, \boldsymbol{\mu}^l, \boldsymbol{\psi}^l$;
 Layer shape parameters: H, W, N, C ;
 Tiling parameters: T_h, T_w, T_n, T_c .
OUTPUT: Loss gradient tensors: $\frac{\partial L}{\partial \mathbf{X}^l}, \frac{\partial L}{\partial \boldsymbol{\gamma}^l}, \frac{\partial L}{\partial \boldsymbol{\beta}^l}$.

```

1: for each tile along  $c$  loop do
    // Computing loss gradients with respect to scale and shift:
2:   Load tiles of  $\boldsymbol{\mu}^l$  and  $\boldsymbol{\psi}^l$ 
3:   for each tile along  $n$  loop do
4:     for each tile along  $w$  loop do
5:       for each tile along  $h$  loop do
6:         Load tiles of  $\mathbf{X}^l$  and  $\frac{\partial L}{\partial \mathbf{X}^{l+1}}$ 
7:         Compute tile of  $\widehat{\mathbf{X}}^l$  (require sub and mul)
8:         Compute partial sums for tiles of  $\frac{\partial L}{\partial \boldsymbol{\gamma}^l}$  and  $\frac{\partial L}{\partial \boldsymbol{\beta}^l}$ 
           (require mul and add)
9:         Store tile of  $\widehat{\mathbf{X}}^l$ 
10:       end for
11:     end for
12:   end for
    // Computing loss gradient with respect to input:
13:   Load tile of  $\boldsymbol{\gamma}^l$ 
14:   Compute the term outside the parenthesis in (28)
     (require mul and div)
15:   for each tile along  $n$  loop do
16:     for each tile along  $w$  loop do
17:       for each tile along  $h$  loop do
18:         Load tiles of  $\widehat{\mathbf{X}}^l$  and  $\frac{\partial L}{\partial \mathbf{X}^{l+1}}$ 
19:         Compute tile of  $\frac{\partial L}{\partial \mathbf{X}^l}$  (require mul and sub)
20:         Store tile of  $\frac{\partial L}{\partial \mathbf{X}^l}$ 
21:       end for
22:     end for
23:   end for
24:   Store tiles of  $\frac{\partial L}{\partial \boldsymbol{\gamma}^l}$  and  $\frac{\partial L}{\partial \boldsymbol{\beta}^l}$ 
25: end for
  
```

individual elements of each tensor (i.e., i to index the elements along the h, w, n loops while j to index the elements along the c loop). Besides, non-bold lower case notations are used to denote individual elements in each tensor, for example, x_{ij}^l indicates an individual element in tensor \mathbf{X}^l .

$$\hat{x}_{ij}^l = (x_{ij}^l - \mu_j^l) \cdot \psi_j^l \quad (25)$$

$$\frac{\partial L}{\partial \boldsymbol{\gamma}_j^l} = \sum_{i=1}^{N_{eff}} \left(\frac{\partial L}{\partial x_{ij}^{l+1}} \cdot \hat{x}_{ij}^l \right) \quad (26)$$

$$\frac{\partial L}{\partial \boldsymbol{\beta}_j^l} = \sum_{i=1}^{N_{eff}} \frac{\partial L}{\partial x_{ij}^{l+1}} \quad (27)$$

$$\frac{\partial L}{\partial x_{ij}^l} = \frac{\boldsymbol{\gamma}_j^l \cdot \boldsymbol{\psi}_j^l}{N_{eff}} \left(N_{eff} \cdot \frac{\partial L}{\partial x_{ij}^{l+1}} - \frac{\partial L}{\partial \boldsymbol{\gamma}_j^l} \cdot \hat{x}_{ij}^l - \frac{\partial L}{\partial \boldsymbol{\beta}_j^l} \right) \quad (28)$$

Unlike most non-Conv layers where the computation comprises one or two kinds of arithmetic operations, the computation of BN_{back} involves several types of arithmetic operations that are embedded within multiple nested loops. Consequently, there are many ways to map the computation of BN_{back} in the generic SIMD processor. In SimDIT, we efficiently schedule the BN_{back} computations in the SIMD array to minimize the number of cycle counts as well as data access cost for the BN_{back} layer. Algorithm 1 summarizes the steps adopted by SimDIT to compute the three loss gradients of the BN_{back} layer. The algorithm shows the computation steps using outer tiles only, which are referred to simply as tiles.

For each channel, the loss gradient computation with respect to input requires the computed loss gradients with respect to scale and shift (Equation (28)). Hence, as shown in Algo-

gorithm 1, we finish computing tiles of $\frac{\partial L}{\partial \boldsymbol{\gamma}^l}$ and $\frac{\partial L}{\partial \boldsymbol{\beta}^l}$ before $\frac{\partial L}{\partial \mathbf{X}^l}$. The BN_{back} computations proceed in two parts:

- (i) Part-1 (Lines 1–12, 24, 25) that computes the $\frac{\partial L}{\partial \boldsymbol{\gamma}^l}$ and $\frac{\partial L}{\partial \boldsymbol{\beta}^l}$ tensors using Equations (25)–(27).
- (ii) Part-2 (Lines 1, 13–23, 25) that computes the $\frac{\partial L}{\partial \mathbf{X}^l}$ tensor using (28).

The processing of Part-1 involves loading tiles of respective input tensors from DRAM (Lines 2 and 6). After computing a tile of $\widehat{\mathbf{X}}^l$, it is stored back to DRAM to be used by Part-2 (Line 9). Since $\widehat{\mathbf{X}}^l$ is a 4D tensor, without this writeback to DRAM, the data will be lost as the computation proceeds along the h, w , and n loops. For the 1D tensors of $\frac{\partial L}{\partial \boldsymbol{\gamma}^l}$ and $\frac{\partial L}{\partial \boldsymbol{\beta}^l}$, the accumulation across the h, w , and n loops gets completed in Line 12 and the data for the corresponding loss gradient tiles are formed. Under the same c loop, these completed tiles of $\frac{\partial L}{\partial \boldsymbol{\gamma}^l}$ and $\frac{\partial L}{\partial \boldsymbol{\beta}^l}$ are reused in Part-2 to compute $\frac{\partial L}{\partial \mathbf{X}^l}$ before they are stored to DRAM (Line 24), reducing off-chip accesses.

During the processing of Part-2, tiles of $\boldsymbol{\gamma}^l, \widehat{\mathbf{X}}^l$, and $\frac{\partial L}{\partial \mathbf{X}^{l+1}}$ are loaded from DRAM (Lines 13 and 18). After computing a tile of the 4D tensor $\frac{\partial L}{\partial \mathbf{X}^l}$, it is stored back to DRAM (Line 20). This is repeated until all three output tensors are computed entirely. The computation of Part-1 and Part-2 requires a series of arithmetic addition (add), subtraction (sub), multiplication (mul), and division (div) operations (Lines 7, 8, 14, and 19).

Using the scheduling steps in Algorithm 1, we develop models for DRAM accesses, SRAM accesses, computation cycles and DRAM stall cycles for the BN_{back} layer. The derivations for these models are presented in Appendix A.

VI. ENERGY AND POWER COMPUTATION

We combine the performance statistics (i.e., cycle counts and number of accesses) from SimDIT with post SP&R power-performance characteristics for a hardware configuration to compute end-to-end execution energy and power of a network. We use the following hardware data from SP&R:

- dynamic and leakage power of systolic PE array (SA) and SIMD array denoted as $\mathcal{P}_{SA-dyn}, \mathcal{P}_{SA-leak}, \mathcal{P}_{SIMD-dyn}$, and $\mathcal{P}_{SIMD-leak}$, respectively.
- per bit access energy for each on-chip buffer (e_{buff}) according to their size specifications.
- effective clock period (T_{clk}).

The total energy to execute a network, E_{total} , is:

$$E_{total} = E_{SA} + E_{SIMD} + E_S + E_D \quad (29)$$

where E_{SA} and E_{SIMD} indicate the energy consumption of the SA and SIMD array, respectively, as they compute a network while E_S and E_D represent data access energy from the on-chip SRAMs and off-chip DRAM, respectively. The energy of the SA and SIMD hardware components include dynamic energy as well as leakage energy and computed as:

$$\begin{aligned}
 E_{SA} &= (\mathcal{C}_{SA} \cdot \mathcal{P}_{SA-dyn} + \mathcal{L}_{total} \cdot \mathcal{P}_{SA-leak}) \cdot T_{clk} \\
 E_{SIMD} &= (\mathcal{C}_{SIMD} \cdot \mathcal{P}_{SIMD-dyn} + \\
 &\quad \mathcal{L}_{total} \cdot \mathcal{P}_{SIMD-leak}) \cdot T_{clk} \quad (30)
 \end{aligned}$$

Here, \mathcal{C}_{SA} [\mathcal{C}_{SIMD}] captures the number of cycles when the SA [SIMD] core actively performs computation while \mathcal{L}_{total}

denotes end-to-end latency (i.e., total number of cycles to execute a network that includes computation as well as stall cycles of the SA and SIMD components). The data access energy from the on-chip SRAMs and off-chip DRAM is:

$$E_S = \sum_{buffer} (A_{S_{buffer}} \cdot e_{buffer}) ; E_D = A_{D_{total}} \cdot e_D \quad (31)$$

Here, $A_{S_{buffer}}$ is the total number of accesses for a buffer $buffer \in \{WBuf, IBuf, OBuf, BBuf, VMem, IMem\}$, and $A_{D_{total}}$ is the total number of accesses from the DRAM with per bit access energy of e_D . Finally, the average power to execute a network is:

$$P_{avg} = E_{total} / (\mathcal{L}_{total} \cdot T_{clk}) \quad (32)$$

VII. EVALUATION

We use SimDIT to analyze the impact of Conv and non-Conv workloads on end-to-end performance of a CNN. We also perform design space exploration to obtain optimized accelerator design solutions. As representative networks, we use ResNet-50, ResNet-18, VGG16, and AlexNet. These are widely used CNN topologies that consist of a diverse set of layers (i.e., Conv, FC, ReLU, Tensor-add, max Pool, global average Pool, and BN). For inference workload, we obtain the network graph containing the tensor specifications of each layer using models from PyTorch (ResNet-50, ResNet-18) and ONNX Model Zoo (VGG16, AlexNet). For training workload, we traverse the inference graph to obtain the tensor specifications of each layer for the forward and backward pass of training. We develop a tiling generator that generates valid tiling parameters for each type of layer using the configuration of the hardware (i.e., the *Hardware Specifications*, summarized in Table II). Since the interface of SimDIT uses tiling parameters as input, they can also be provided externally by the user (for example, valid tiling parameters generated by an external compiler).

To obtain the backend hardware data, we use RTL of GeneSys from VeriGOOD-ML open-source repository [20], an automated Verilog generator for ASIC-based DNN accelerator. We perform backend synthesis place-and-route of various GeneSys designs (both inference and training hardware designs) using a commercial 12nm technology node to obtain the post SP&R power performance characteristics of the hardware. We use a commercial memory compiler to obtain the per bit access energy of the on-chip SRAMs. The per bit access energy of HBM2 DRAM memory is obtained from [21].

TABLE VI: Percentage of runtime, energy, and number of data accesses for the non-Conv layers with respect to total network performance (i.e., Conv + non-Conv) for ResNet-50 during training and inference.

$J \times K$	non-Conv runtime	non-Conv on-chip access	non-Conv off-chip access	non-Conv energy	Total power	Total runtime
Training (per iteration)						
16×16	41.9%	4.1%	44.8%	50.3%	0.63W	6.86s
32×32	56.6%	4.1%	59.3%	52.3%	1.58W	2.54s
64×64	59.5%	2.7%	56.2%	49.4%	3.94W	1.21s
Inference (per image)						
16×16	30.1%	1.9%	38.7%	33.2%	0.46W	0.028s
32×32	41.6%	2.0%	54.4%	40.3%	1.02W	0.010s
64×64	49.3%	1.8%	56.6%	38.2%	2.55W	0.004s

A. Impact of Conv and non-Conv Operations

Table VI demonstrates the fraction of runtime, energy, and number of on-chip and off-chip accesses for the non-Conv layers of ResNet-50 with respect to the total network performance across different hardware configurations. The table also presents the total power and runtime to execute the network (last two columns).

For training, the evaluations are shown for a single iteration through the network (i.e., a forward pass + a backward pass) using a batch size of 32 on three hardware configurations:

HT1 Array size = 16×16

[$W_{buf}, I_{buf}, O_{buf}, V_{mem}$] = [256, 128, 256, 256] kB

Bandwidth per off-chip interface = 128 bits/cycle

HT2 Array size = 32×32

[$W_{buf}, I_{buf}, O_{buf}, V_{mem}$] = [512, 256, 512, 512] kB

Bandwidth per off-chip interface = 256 bits/cycle

HT3 Array size = 64×64

[$W_{buf}, I_{buf}, O_{buf}, V_{mem}$] = [1024, 512, 1024, 1024] kB

Bandwidth per off-chip interface = 512 bits/cycle

Following [1], across all three hardware substrates, we use 16 bits for ifmap/weight and 32 bits for psum data on the systolic PE array, and 32 bits for all input/output data of the SIMD array. From Table VI, across all three hardware configurations, the energy and runtime spent to execute the non-Conv layers are a significant fraction of the network performance e.g., up to 59.5% runtime and 52.3% energy are consumed by the non-Conv layers. This is not surprising since the training workload comprises a large set of non-Conv layers. As listed in Table I, there are four types of non-Conv layers during the forward pass of training while it consists of five categories of non-Conv layers during the backward pass.

For the inference workload, the evaluations in Table VI are shown for a single inference using a batch size of 1. Similar to [10], the inference hardware uses 8-bit for ifmap/weight and 32-bit for psum on the SA component while 32-bit data on the SIMD component. The inference results are shown using three hardware configurations with different array sizes, SRAM specifications, and off-chip bandwidths:

HI1 Array size = 16×16

[$W_{buf}, I_{buf}, O_{buf}, V_{mem}$] = [32, 32, 128, 128] kB

Bandwidth per off-chip interface = 128 bits/cycle

HI2 Array size = 32×32

[$W_{buf}, I_{buf}, O_{buf}, V_{mem}$] = [256, 128, 512, 512] kB

Bandwidth per off-chip interface = 256 bits/cycle

HI3 Array size = 64×64

[$W_{buf}, I_{buf}, O_{buf}, V_{mem}$] = [512, 256, 1024, 1024] kB

Bandwidth per off-chip interface = 512 bits/cycle

It is evident that the runtime and energy overheads from the non-Conv layers are comparable to that of Conv layers. While the overheads are smaller for HI1, with larger array size, as the ratio of the computing elements (i.e., #of PEs vs. #of ALUs) in the 2D SA vs. 1D SIMD component increases, the performance overheads from non-Conv layers increases, e.g., 49.3% runtime and 38.2% energy of HI3 for non-Conv layers.

For a similar analysis on ResNet-18, Table VII summarizes the fraction of runtime, energy, on-chip, and off-chip accesses for the non-Conv layers with respect to the total network

TABLE VII: Percentage of runtime, energy, and number of data accesses for the non-Conv layers with respect to total network performance for ResNet-18 during training and inference.

$J \times K$	non-Conv runtime	non-Conv on-chip access	non-Conv off-chip access	non-Conv energy	Total power	Total runtime
Training (per iteration)						
16×16	30.5%	2.7%	41.8%	42.7%	0.57W	2.50s
32×32	41.8%	2.4%	60.0%	40.9%	1.56W	0.91s
64×64	45.4%	1.5%	56.1%	36.9%	4.22W	0.42s
Inference (per image)						
16×16	17.4%	1.2%	31.3%	24.1%	0.36W	0.011s
32×32	24.7%	1.1%	46.0%	26.6%	0.91W	0.004s
64×64	30.0%	0.9%	46.5%	22.0%	2.64W	0.002s

performance while executed on HT1, HT2, HT3 for training and HI1, HI2, HI3 for inference. Similar trends are seen for ResNet-18 where non-Conv layers constitute comparable runtime and energy overheads to that of Conv layers: e.g., 17.4%–45.4% overhead in runtime while 22.0%–42.7% overhead in energy across the inference and training workloads.

B. Design Space Exploration

Optimal allocation of hardware resources: We use SimDIT to perform design space exploration (DSE) to optimally distribute various hardware resources for inference workload. Under specified budgets for total on-chip SRAM size and total available off-chip bandwidth, we exhaustively search the design space by varying 8 parameters (i.e., sizes and bandwidths for WBuf, IBuf, OBuf, and VMem) while all hardware points lie within 15% deviation from the budget constraints to allow greater flexibility to find the optimum. We use 8-bit ifmap/weight and 32-bit psum for SA, and 32-bit data for the SIMD component.

Table VIII shows the optimal distribution of hardware resources across four different sizes of $J \times K$ for ResNet-50 inference using budget constraint pair of (512kB, 512 bits/cycle), (1024kB, 1024 bits/cycle), (2048kB, 2048 bits/cycle), and (4096kB, 4096 bits/cycle) for the 16×16, 32×32, 64×64, and 128×128 array, respectively. The DSE uses number of total network execution cycles as the performance metric.

TABLE VIII: Performance comparison of optimal hardware allocation with worst-case allocation for ResNet-50 inference workload across four different array sizes.

$J \times K$	Optimal resource allocation		Improvement over worst-case allocation
	SARM sizes (kB) [Wbuf, Ibuf, Obuf, Vmem]	Bandwidth (bits/cycle) [BW _w , BW _i , BW _o , BW _v]	
16×16	[128, 256, 64, 64]	[64, 64, 128, 256]	9.64×
32×32	[256, 256, 128, 256]	[128, 128, 256, 512]	14.45×
64×64	[256, 512, 256, 1024]	[256, 256, 512, 1024]	18.43×
128×128	[512, 512, 512, 2048]	[512, 512, 1024, 2048]	25.55×

TABLE IX: Performance comparison of optimal hardware allocation with worst-case allocation for inference workload on a 64×64 array using budget constraint pair of (2048kB, 2048 bits/cycle) across different networks.

Network	Optimal resource allocation		Improvement over worst-case allocation
	SARM sizes (kB) [Wbuf, Ibuf, Obuf, Vmem]	Bandwidth (bits/cycle) [BW _w , BW _i , BW _o , BW _v]	
ResNet-18	[512, 128, 128, 1024]	[512, 256, 256, 1024]	13.85×
VGG16	[512, 256, 512, 512]	[512, 256, 256, 1024]	19.94×
AlexNet	[1024, 256, 128, 512]	[512, 256, 256, 1024]	33.72×

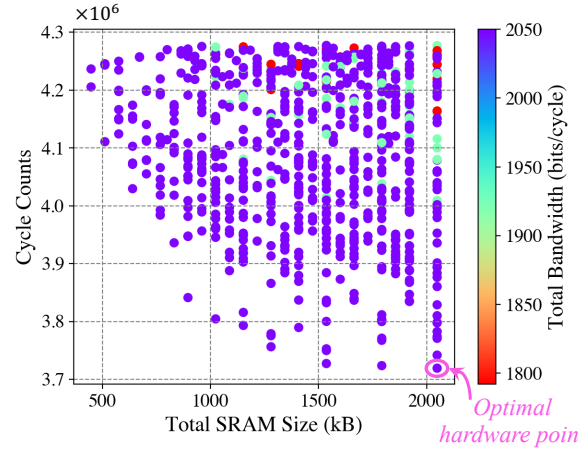


Fig. 11: Distribution of cycle counts vs. total SRAM size and total bandwidth for various hardware points with maximum 15% performance penalty with respect to optimal (64×64 array, ResNet-50 inference workload). The third axis of the plot (i.e., total bandwidth) is indicated by color heatmap.

TABLE X: Performance comparison of optimal hardware point with economic design solutions for ResNet-50 inference on 64×64 array.

Hardware point	Total SRAM size (kB) [Wbuf, Ibuf, Obuf, Vmem]	Total bandwidth (bits/cycle) [BW _w , BW _i , BW _o , BW _v]	Penalty w.r.t. optimal
Optimal	2048 [256, 512, 256, 1024]	2048 [256, 256, 512, 1024]	–
Minimized SRAM size	448 [128, 128, 128, 64]	2048 [256, 256, 512, 1024]	13.1%
Minimized bandwidth	1024 [256, 256, 256, 256]	1792 [256, 256, 256, 1024]	14.6%

The rightmost column shows the improvement of optimal hardware point as compared to the worst-case allocation, and thus, represents the best-case to worst-case performance range. The large performance range underscores the importance of optimal distribution of hardware resources, for example, if the hardware resource allocation is not optimized by careful analysis, there can be a performance penalty of up to 18.43× on the 64×64 array. Similar performance penalty is observed for ResNet-18, VGG16, and AlexNet. For these three networks, optimal hardware parameters are shown in Table IX for a 64×64 array, where, for example, VGG16 demonstrates a performance penalty of up to 19.94×.

Design landscape analysis: We now analyze the flatness of the design space around the optimal hardware point for the 64×64 array under the budget boundaries of 2048kB SRAM and 2048 bits/cycle off-chip bandwidth using ResNet-50. This analysis enables finding economic design solutions at the cost of small penalty in performance. Fig. 11 shows the distribution of cycle counts for all the hardware points for which the performances are within 15% of the optimal cycle counts. It is clear that there are many design points that deliver performance close to the optimal using a smaller hardware resource (i.e., on-chip memory size and/or off-chip bandwidth) as compared to the optimal hardware point.

Table X presents the performance comparison of the optimal hardware point with two economic design solutions that are obtained from the hardware points in Fig. 11. The design that minimizes the on-chip SRAM size saves 78.1% memory cost

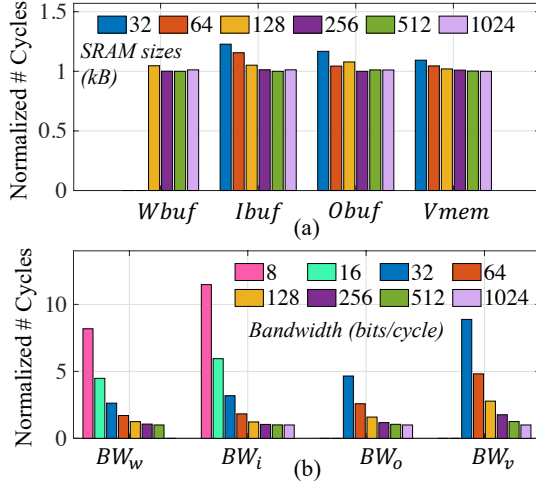


Fig. 12: Normalized cycle counts of ResNet-50 inference on 64×64 array with (a) various SRAM sizes and (b) various off-chip bandwidth parameters. (a missing bar indicates a hardware point that is not valid due to minimum/maximum size constraint on the respective hardware parameter).

over the optimum with only a 13.1% penalty in performance. Another design point that minimizes the off-chip bandwidth uses 50% less memory and 12.5% less bandwidth as compared to the optimal point with only a 14.6% penalty in performance.

Sensitivity analysis: Finally, we perform sensitivity analysis to determine how each of the SRAM sizes and off-chip bandwidth parameters impacts the performance. Fig. 12 shows the cycle counts of ResNet-50 inference for 64×64 array (normalized to the cycle counts of the optimal hardware point obtained from Table VIII). In (a), the results are shown by varying one SRAM size parameter at a time while keeping the remaining seven parameters same as the optimal configuration point (the small amount of non-monotonicity in the bars of (a) can be attributed to the tiling algorithm). Similar results are shown in (b) by varying one off-chip bandwidth parameter at a time. It is evident from (a) that the cycle counts have small sensitivity to the SRAM size parameters. For example, the smallest $Ibuf$ increases the cycle counts $1.23 \times$ from the optimal while the performance saturates quickly with an increment in $Ibuf$. The bars in (b) demonstrate that the performance is highly sensitive to the off-chip bandwidth parameters. For example, the smallest BW_i shows $11.4 \times$ increment in cycle counts while the saturation starts from 256 bits/cycle bandwidth.

The Conv layers in the SA offer ample opportunity for data reuse, hence, changing one buffer size from the optimal configuration point does not impact the performance of SA significantly. Besides, since there is nearly zero data reuse opportunity in the non-Conv layers, the size of VMem minimally affects the DRAM access count and, thus, has small impact on the performance of the SIMD array. In contrast, since the bandwidth parameters dictate the costly data communication time with the off-chip DRAM, the performance is largely affected by these parameters.

VIII. CONCLUSION

A comprehensive simulation framework covering convolution and a diverse set of non-convolution operations for DNN inference and training on ASIC accelerator platforms has been proposed. The detailed performance statistics provided by the simulator have been integrated with a backend flow to obtain end-to-end energy, runtime, and power of executing a network. Performance analysis using ResNet-50 and ResNet-18 training workloads reveals that non-convolution operations constitute a significant fraction of network runtime and energy. Design space exploration has been performed to identify optimal and economic inference design solutions under specified on-chip SRAM and off-chip bandwidth budgets. Optimal distribution of hardware resources is shown to offer substantial performance gain over generic static hardware resource allocation. In addition, economic design solutions are demonstrated to save remarkable memory footprint over the optimal hardware point at the cost of a small penalty in performance.

ACKNOWLEDGMENTS

This work is supported in part by AFRL under the DARPA RTML program (award FA8650-20-2-7009). The U. S. government (USG) is authorized to reproduce and distribute reprints for governmental purposes notwithstanding any copyright notation thereon. The views and conclusions contained herein are those of the authors and should not be interpreted as necessarily representing the official policies or endorsements, either expressed or implied, of AFRL, DARPA, or USG.

APPENDIX

A. Data Access and Cycle Count Models for BN_{back}

The data access and cycle count models of SimDIT for BN_{back} layer using the steps in Algorithm 1 is outlined here. We present the derivations for Part-2. Similar models are developed for Part-1. The computation of BN_{back} proceeds along the four computation loops (i.e., h, w, n, c). We define four multipliers to express the iterations⁵ along these loops as follows (the tiling template is shown in Fig. 10):

$$m_h = \frac{H}{T_h} ; m_w = \frac{W}{T_w} ; m_n = \frac{N}{T_n} ; m_c = \frac{C}{T_c} \quad (33)$$

Number of DRAM accesses: There are two types of tensors in BN_{back} : 4D and 1D. The volume of a tile for a 4D tensor, \mathcal{V}_{tile}^{4D} , is given by $(T_h \cdot T_w \cdot T_n \cdot T_c)$ while the volume of a 1D tensor tile, \mathcal{V}_{tile}^{1D} , equals T_c . During the computation of Part-2, each tiles of γ^l (one 1D tensor), $\tilde{\mathbf{X}}^l$, $\frac{\partial L}{\partial \tilde{\mathbf{X}}^{l+1}}$, and $\frac{\partial L}{\partial \tilde{\mathbf{X}}^l}$ (three 4D tensors) are loaded/stored from/to DRAM once. Therefore, the number of DRAM access for Part-2 to compute the entire output tensor of $\frac{\partial L}{\partial \tilde{\mathbf{X}}^l}$ is given by:

$$A_{D_{Part-2}} = (\mathcal{V}_{tile}^{1D} + 3\mathcal{V}_{tile}^{4D}(m_h m_w m_n)) m_c b_{io} \quad (34)$$

Here, b_{io} is the data bit-width for all input and output tensors⁶.

⁵Similar to Tensor-add layer, we present the models for BN_{back} using outer tiles only, and all tiles and computation iterations correspond to outer tiles in this appendix.

⁶While the implementation of SimDIT accounts for separate bit-widths for input and output data, we use a single bit-width for clarity of the presented equations for BN_{back} .

Number of SRAM accesses: To compute the term outside the parenthesis in (28), one mul and one div operations per element of an 1D tile is required resulting in $2\mathcal{V}_{tile}^{1D}$ number of arithmetic operations. To compute the term inside the parenthesis and combine it with the term outside the parenthesis, three mul and two sub operations per element of a 4D tile is required. This leads to $5\mathcal{V}_{tile}^{4D}$ number of arithmetic operations. The total number of op count to process entire Part-2 is, therefore, computed by (35). For each arithmetic operation, three VMem accesses are required (i.e., read access for two operands and write access for one operand). Hence, the number of SRAM accesses for Part-2 is computed from the op count using (36).

$$\text{op count} = (2\mathcal{V}_{tile}^{1D} + 5\mathcal{V}_{tile}^{4D} \cdot (m_h m_w m_n)) m_c \quad (35)$$

$$A_{SPart-2} = \text{op count} \cdot (2 + 1) \cdot b_{io} \quad (36)$$

Number of computation cycles: The SIMD array performs K arithmetic operations in parallel where each ALU requires λ_ω cycles to complete an arithmetic operation ω . Hence, the number of cycles to compute an 1D tile and a 4D tile of output (Lines 14 and 19 of Algorithm 1) are computed using Equations (37) and (38), respectively, where, as in Tensor-add, the c dimension is mapped along the ALUs of the SIMD array.

$$\mathcal{C}_{tile}^{1D} = \left\lceil \frac{T_c}{K} \right\rceil \cdot (\lambda_{mul} + \lambda_{div}) \quad (37)$$

$$\mathcal{C}_{tile}^{4D} = (T_h T_w T_n) \cdot \left\lceil \frac{T_c}{K} \right\rceil \cdot (3\lambda_{mul} + 2\lambda_{sub}) \quad (38)$$

The tiled computations are iterated across the four loops to compute the entire $\frac{\partial L}{\partial \mathbf{X}^l}$ tensor. The total number of computation cycles, including pipeline setup overhead, for Part-2 is:

$$\mathcal{C}_{Part-2} = [(\mathcal{C}_{tile}^{4D} + PSOSIMD) (m_h m_w m_n) + \mathcal{C}_{tile}^{1D}] m_c$$

Number of stall cycles: The SIMD array is stalled during the load and store operations of each tile. Thus, using the tiled volumes of data and off-chip bandwidth for VMem, the number of stall cycles to process Part-2 is computed by:

$$\mathcal{S}_{Part-2} = \left(\left\lceil \frac{\mathcal{V}_{tile}^{1D} \cdot b_{io}}{BW_v} \right\rceil + \left\lceil \frac{3\mathcal{V}_{tile}^{4D} \cdot b_{io}}{BW_v} \right\rceil (m_h m_w m_n) \right) m_c$$

REFERENCES

- [1] N. P. Jouppi, D. H. Yoon, G. Kurian, S. Li, N. Patil, J. Laudon, C. Young, and D. Patterson, "A Domain-Specific Supercomputer for Training Deep Neural Networks," *Communications of the ACM*, vol. 63, no. 7, pp. 67–78, July 2020.
- [2] A. Samajdar, Y. Zhu, P. Whatmough, M. Mattina, and T. Krishna, "SCALE-Sim: Systolic CNN Accelerator Simulator," *arXiv:1811.02883*, 2018.
- [3] A. Parashar, P. Raina, Y. S. Shao, Y.-H. Chen, V. A. Ying, A. Mukkara, R. Venkatesan, B. Khailany, S. W. Keckler, and J. Emer, "Timeloop: A Systematic Approach to DNN Accelerator Evaluation," in *Proceedings of the IEEE International Symposium on Performance Analysis of Systems and Software*, 2019, pp. 304–315.
- [4] H. Kwon, P. Chatarasi, V. Sarkar, T. Krishna, M. Pellauer, and A. Parashar, "MAESTRO: A Data-Centric Approach to Understand Reuse, Performance, and Hardware Cost of DNN Mappings," *IEEE Micro*, vol. 40, no. 3, pp. 20–29, 2020.
- [5] S. D. Manasi and S. S. Sapatnekar, "DeepOpt: Optimized Scheduling of CNN Workloads for ASIC-based Systolic Deep Learning Accelerators," in *Proceedings of the Asia-South Pacific Design Automation Conference*, Jan. 2021, pp. 235–241.
- [6] T.-J. Yang, Y.-H. Chen, J. Emer, and V. Sze, "A Method to Estimate the Energy Consumption of Deep Neural Networks," in *Asilomar Conference on Signals, Systems, and Computers*, 2017, pp. 1916–1920.
- [7] Y. Ma, Y. Cao, S. Vruthula, and J. Seo, "Performance Modeling for CNN Inference Accelerators on FPGA," *IEEE Transactions on Computer-Aided Design of Integrated Circuits and Systems*, vol. 39, no. 4, pp. 843–856, April 2020.
- [8] P. Xu, X. Zhang, C. Hao, Y. Zhao, Y. Zhang, Y. Wang, C. Li, Z. Guan, D. Chen, and Y. Lin, "AutoDNNchip: An Automated DNN Chip Predictor and Builder for Both FPGAs and ASICs," in *Proceedings of the ACM/SIGDA International Symposium on Field-Programmable Gate Arrays*, 2020, p. 40–50.
- [9] Y. Qi, S. Zhang, and T. M. Taha, "TRIM: A Design Space Exploration Model for Deep Neural Networks Inference and Training Accelerators," *IEEE Transactions on Computer-Aided Design of Integrated Circuits and Systems*, pp. 1–1, 2022.
- [10] N. P. Jouppi *et al.*, "In-datacenter Performance Analysis of a Tensor Processing Unit," in *Proceedings of the ACM International Symposium on Computer Architecture*, Jun. 2017, pp. 1–12.
- [11] H. Esmaeilzadeh, S. Ghodrati, J. Gu, S. Guo, A. B. Kahng, J. K. Kim, S. Kinzer, R. Mahapatra, S. D. Manasi, E. Mascarenhas, S. S. Sapatnekar, R. Varadarajan, Z. Wang, H. Xu, B. R. Yatham, and Z. Zeng, "VeriGOOD-ML: An Open-Source Flow for Automated ML Hardware Synthesis," in *Proceedings of the IEEE/ACM International Conference on Computer-Aided Design*, 2021.
- [12] H. Genc, S. Kim, A. Amid, A. Haj-Ali, V. Iyer, P. Prakash, J. Zhao, D. Grubb, H. Liew, H. Mao, A. Ou, C. Schmidt, S. Steffl, J. Wright, I. Stoica, J. Ragan-Kelley, K. Asanovic, B. Nikolic, and Y. S. Shao, "Gemmini: Enabling Systematic Deep-Learning Architecture Evaluation via Full-Stack Integration," in *Proceedings of the ACM/IEEE Design Automation Conference*, 2021, pp. 769–774.
- [13] T. Moreau, T. Chen, L. Vega, J. Roesch, E. Yan, L. Zheng, J. Fromm, Z. Jiang, L. Ceze, C. Guestrin, and A. Krishnamurthy, "A Hardware-Software Blueprint for Flexible Deep Learning Specialization," *IEEE Micro*, vol. 39, no. 5, pp. 8–16, 2019.
- [14] "SimDIT: A simulation framework for DNN inference and training on ASIC accelerator platforms," <https://github.com/VeriGOOD-ML/public/tree/main/genesys/SimDIT>.
- [15] S. Banerjee, S. Burns, P. Cocchini, A. Davare, S. Jain, D. Kirkpatrick, A. Sorokin, J. Yang, and Z. Yang, "A Highly Configurable Hardware/Software Stack for DNN Inference Acceleration," *arXiv preprint arXiv:2111.15024*, Nov. 2021.
- [16] A. Krizhevsky, I. Sutskever, and G. E. Hinton, "ImageNet Classification with Deep Convolutional Neural Networks," in *Advances in Neural Information Processing Systems*, 2012, pp. 1097–1105.
- [17] K. He, X. Zhang, S. Ren, and J. Sun, "Deep Residual Learning for Image Recognition," in *Proceedings of the IEEE Conference on Computer Vision and Pattern Recognition*, Jun. 2016.
- [18] S. Ioffe and C. Szegedy, "Batch Normalization: Accelerating Deep Network Training by Reducing Internal Covariate Shift," in *Proceedings of the International Conference on Machine Learning*, vol. 37, July 2015, pp. 448–456.
- [19] Y. Lecun, L. Bottou, Y. Bengio, and P. Haffner, "Gradient-based learning applied to document recognition," *Proceedings of the IEEE*, vol. 86, no. 11, pp. 2278–2324, 1998.
- [20] "VeriGOOD-ML," <https://github.com/VeriGOOD-ML/public>.
- [21] M. O'Connor, N. Chatterjee, D. Lee, J. Wilson, A. Agrawal, S. W. Keckler, and W. J. Dally, "Fine-Grained DRAM: Energy-Efficient DRAM for Extreme Bandwidth Systems," in *Proceedings of the IEEE/ACM International Symposium on Microarchitecture*, 2017, p. 41–54.